Dramatic pressure-sensitive ion conduction in conical nanopores

Laetitia Jubin[a,1], Anthony Poggioli[a,1], Alessandro Siria[a], and Lydéric Bocquet[a,2]

[a]Laboratoire de Physique Statistique, Ecole Normale Supérieure, 75005 Paris, France

Ion transporters in Nature exhibit a wealth of complex transport properties such as voltage gating, activation, and mechanosensitive behavior. When combined, such processes result in advanced ionic machines achieving active ion transport, high selectivity, or signal processing. On the artificial side, there has been much recent progress in the design and study of transport in ionic channels, but mimicking the advanced functionalities of ion transporters remains as yet out of reach. A prerequisite is the development of ionic responses sensitive to external stimuli. In the present work, we report a counterintuitive and highly nonlinear coupling between electric and pressure-driven transport in a conical nanopore, manifesting as a strong pressure dependence of the ionic conductance. This result is at odds with standard linear response theory and is akin to a mechanical transistor functionality. We fully rationalize this behavior on the basis of the coupled electrohydrodynamics in the conical pore by extending the Poisson–Nernst–Planck–Stokes framework. The model is shown to capture the subtle mechanical balance occurring within an extended spatially charged zone in the nanopore. The pronounced sensitivity to mechanical forcing offers leads in tuning ion transport by mechanical stimuli. The results presented here provide a promising avenue for the design of tailored membrane functionalities.

nanofluidics | nonlinear transport | conical nanopores | mechanosensitivity

I onic transport in nanometric-scale channels and pores has been an intense topic of research for two decades (1, 2), highlighting novel transport processes at the nanoscale (1, 2), with applications to, e.g., physical modeling of biological channels (3, 4), energy generation (1, 5–8), and desalination (9). Coupling of electrostatic and electrodiffusive processes at the nanoscale can result in ionic current rectification, in analogy with classical solid-state semiconductor diodes (1, 10–14). Diode-like behavior of the ionic current can be harvested for applications such as solvent rectification and desalination (9, 15–18), counter-gradient ionic pumping (19), and energy harvesting (20).

However, the ability to tune the ionic conduction by an external stimulus, exhibited in biological nanopores (21–24), remains challenging to achieve artificially. The nanofluidic equivalent of the transistor, pioneered by refs. 25 and 26, still poses many difficulties for efficient implementation in nanofluidic circuitry. More generally, the nonlinear response of ionic transport in nanopores to external forcings and its relation to the nanopore geometry remain poorly understood. Diode-like behavior highlights a rectified current–voltage response in asymmetric nanopores, but the extension to driving forces other than the electric forcing remains largely unexplored up to now. Of particular interest is the coupling of ionic transport to mechanical forcings—e.g., an imposed pressure drop—beyond the linear response regime. The ability to tune the conduction by such an external stimulus would open up the possibility of designing advanced fluidic circuitry, such as the hypothetical memristor response (27). However, the low Reynolds number hydrodynamics governing nanometric fluid transport are by essence time reversible and resolutely linear in pressure forcing, suggesting the a priori impossibility of a nonlinear mechanical response. Accordingly the ionic

response to mechanical driving is usually described in terms of a streaming current that is linear in pressure drop and verifies the Onsager symmetry relations (1).

In this paper, we report observations of ionic transport in conical nanocapillaries demonstrating a considerable nonlinear sensitivity of ionic conduction to applied pressure. This results in an ionic conductance that exhibits a nonanalytic increase or decrease with pressure, allowing for robust and versatile tuning of the conductance. Even more striking is the fact that this behavior is observed for small imposed pressure drops, while the classical linear response is recovered at large imposed pressure drops, at odds with the expected linear response scenario. We rationalize these observations on the basis of a theoretical framework based on the coupled electromechanical dynamics in the conical nanopore. It demonstrates the role played by the pressure-induced modifications of the spatially charged zone (SCZ) that forms in the interior of the nanopore and is at the origin of the highly nonlinear current response.

Experiments

We conducted experiments on conical glass nanocapillaries, which constitute easily fabricated and readily reproducible physical models of a single conical nanopore. The interior radius of these nanocapillaries varied between 250 μm on the upstream end and 165 ± 15 nm at the tip over a length of ~ 3 mm, corresponding to a half angle of approximately $5°$. (Fig. 1B and *SI Materials and Methods*). During the experiments, ionic current was measured as a function of applied voltage ($-400 < \Delta V < +400$ mV) and pressure ($0 < \Delta P < 1,500$ mbar) at a fixed ionic concentration c_0 of potassium chloride (KCl), as illustrated in Fig. 1A and detailed in *Materials and Methods*.

Fig. 1. Experimental setup with a single conical nanopore and experimental response of the ionic current I to applied voltage ΔV and pressure ΔP. (A) Sketch. (B) SEM image. (C) Current–voltage curves for increasing values of ΔP, as indicated in the key. *Inset* shows the current as a function of ΔP for several different values of ΔV, colored according to the key in *D*. (D) Additional current induced by applied pressure, I_P, as a function of ΔP for several different values of ΔV, as indicated in the key. The arrow indicates I_{offset}, the offset in I_P compared with the linear response obtained for $\Delta V = 0$, for -400 mV. The experimental data are fitted according to Eq. **1** (solid lines). All measurements correspond to a molarity $[\text{KCl}] = 10^{-3}$ M, pH $\simeq 6$, and a nominal tip radius of $R_0 = 165 \pm 15$ nm.

The results of experiments conducted at a molarity $[\text{KCl}] = 10^{-3}$ M and pH ≈ 6 are shown in Fig. 1 *C* and *D*. At this concentration and pH, we observe substantial rectification of the current–voltage (IV) curve for $\Delta P = 0$ (Fig. 1*C*), in agreement with previous observations (17, 28, 29). Conversely, for $\Delta V = 0$, the pressure-driven response behaves as expected and a streaming current is generated, linear in ΔP (Fig. 1*C*, *Inset*) (1, 2, 30). This streaming current originates from the pressure-induced advection of ions within the Debye screening layer that forms in the vicinity of solid–liquid interfaces (2). It is given by the Smoluchowski result, which, in a conical nanopore with linearly varying radius of slope α_1, takes the form $I_{\text{stm}} = \pi R_0 \alpha_1 \mu_{\text{EO}} \times \Delta P$, where R_0 is the minimum radius occurring at the tip of the nanopore, and $\mu_{\text{EO}} \equiv (\epsilon/\eta)(-\zeta)$ is the electroosmotic mobility. In the latter quantity, ζ is the so-called zeta potential, and η and ϵ are the water viscosity and dielectric constant, respectively. Quantitatively, the streaming conductance $S_{\text{stm}} = I_{\text{stm}}/\Delta P$ obtained at zero applied voltage is $S_{\text{stm}}^{\text{exp}} = 0.153$ nA $\cdot$ bar^{-1}, corresponding to a zeta potential of $\zeta \simeq -42$ mV in agreement with the literature (31). Incidentally, by comparing the above expression for the streaming current to the classical result obtained for a cylindrical geometry, $I_{\text{stm}} = (\pi R_0^2/L)\mu_{\text{EO}} \times \Delta P$, we find that the gradient is confined to an effective length of the order $L_{\text{eff}} = R_0/\alpha_1$.

The behavior for combined finite ΔV and ΔP differs dramatically from the behavior observed when only one forcing is nonzero. As shown in Fig. 1*C*, the IV response changes qualitatively for increasing applied pressures, linearizing for pres-

sures $\gtrsim 200$ mbar. Similarly, for a given applied voltage drop ΔV, the current–pressure (IP) response is dramatically nonlinear for small pressures $\Delta P \lesssim 50$ mbar. As shown in Fig. 1*D*, this nonlinearity is particularly apparent if we examine the additional current induced by pressure, $I_P \equiv I(\Delta P, \Delta V) - I(\Delta P = 0, \Delta V)$, as a function of ΔP for fixed values of ΔV. As shown in Fig. 1*D*, for any voltage drop the pressure dependence of I_P is well described by a simple expression of the form

$$I_P(\Delta P) = S_{\text{stm}}\Delta P + I_{\text{offset}} \frac{a_1 \Delta P^{1/2} + a_2 \Delta P}{1 + a_1 \Delta P^{1/2} + a_2 \Delta P}, \quad [1]$$

where the fitting coefficients a_i and I_{offset} are functions of the voltage drop ΔV. This highlights a small pressure response of the current that scales as $I_P \sim \Delta P^{1/2}$, while the linear regime $I_P \sim \Delta P$ is recovered for large pressure. The square-root dependence of the ionic current on pressure as $\Delta P \to 0$ suggests that the response is nonanalytic at $\Delta P = 0$, within the accuracy of the experiments. This response is obviously at odds with naive considerations, which would rather suggest that the pressure-induced response at small ΔP should take the form of a Taylor expansion in odd powers of ΔP, $I_P \simeq b_1 \Delta P + b_3 \Delta P^3 + \ldots$, where the coefficients of the expansion may themselves be expressed as (even) analytic expansions in ΔV. As highlighted by Fig. 1*D*, the response to mechanoelectric driving forces is highly nonlinear and far stronger than such considerations would suggest.

Surprisingly, while the pressure response observed here is highly nonlinear for small ΔP (and any finite ΔV), the limiting slope of the IP curves obtained for large ΔP is independent of voltage and equal to the slope obtained when $\Delta V = 0$ V (Fig. 1*D*). In this large ΔP regime, the IP response is again characterized by a linear relationship, but now with a voltage-dependent offset current (Eq. **1**). The offset current represents a substantial enhancement of the streaming current that would be obtained in the ordinary linear response regime; this can be seen by comparing the linear IP curves corresponding to $\Delta V = 0$ and -400 mV (Fig. 1*D*).

Finally, we note that this drastically nonlinear behavior is obtained when no Debye-layer overlap occurs in the nanocapillary; the Debye layer here is ~ 10 nm thick, an order of magnitude smaller than the minimum nanocapillary radius, $R_0 = 165 \pm 15$ nm.

Altogether, these results are best described in terms of a pressure-dependent ionic conductance. We report in Fig. 2*A* and *B*, respectively, both the apparent conductance $G_{\text{app}} \equiv \Delta I/\Delta V$ and the differential conductance $G_{\text{diff}} \equiv \partial I/\partial V$. Both quantities highlight a strong sensitivity of the conductance to pressure for small applied pressures. Depending on the applied voltage, the conductance increases or decreases with ΔP, with variations of up to 100% for a change of pressure as small as 100 mbar. The result is an ionic conduction that is dramatically dependent on external mechanical conditions.

Model

To rationalize the a priori unexpected experimental results presented above, we have developed a one-dimensional model of the ionic transport based on the radially integrated Poisson, Nernst–Planck, and Stokes equations for the electrostatic field, ionic fluxes and concentrations, and the pressure and hydrodynamic velocity, respectively. Radial integration of the Nernst–Planck and Stokes equations typically proceeds on the assumption of a local Poisson–Boltzmann equilibrium (1, 2, 7). Such an equilibrium requires local electroneutrality, with the integrated ionic charge density exactly balancing the local surface charge density everywhere. However, in the present
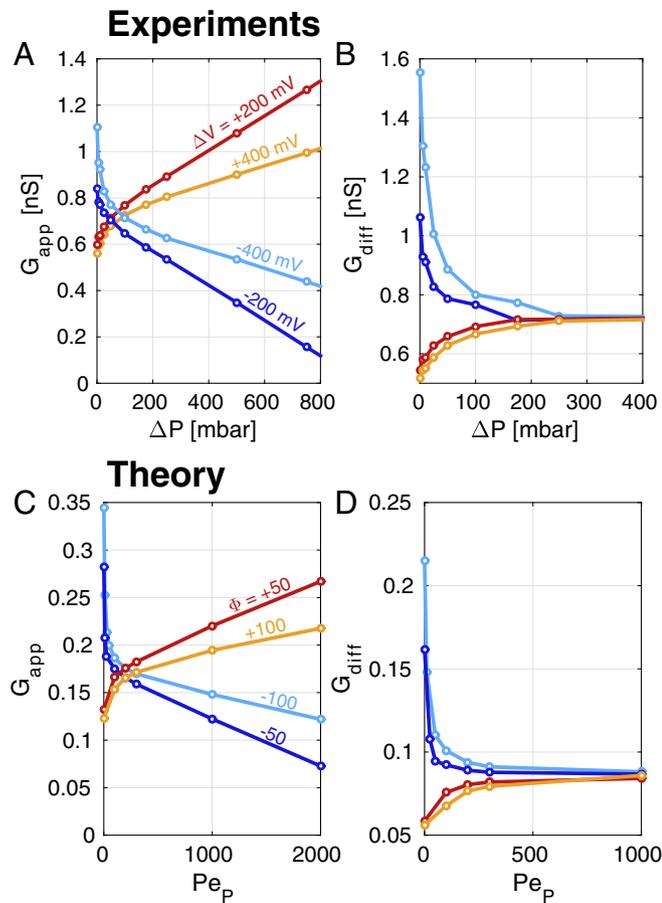
Fig. 2. Experimental (*A* and *B*) and model-derived (*C* and *D*) effective (*A* and *C*) and differential (*B* and *D*) conductance as a function of applied pressure for several different values of applied voltage. The corresponding values of ΔV (Φ) are indicated in *A* (*C*). Φ and Pe_P are the dimensionless rescaled voltage and pressure, respectively, and are defined in the main text.

model, we allow for small deviations from local equilibrium with the possibility of nonelectroneutral regions, so-called SCZs. These deviations are characterized by a local net charge δn_c, defined as

$$\delta n_c \equiv n_c + \mathrm{S}\frac{2\mathrm{Du}_0}{R}, \qquad [2]$$

where n_c is the local volume density of ionic charge, nondimensionalized by ec_0; e is the elementary charge; c_0 is the ionic concentration in the reservoirs; $\mathrm{S}=-1$ is the sign of the surface charge for glass (31); R is the local radius, nondimensionalized by the minimum value R_0; and the Dukhin number is defined in terms of the magnitude of the surface charge $|\sigma|$, the reservoir concentration, and the minimum radius as

$$\mathrm{Du}_0 \equiv \frac{|\sigma|}{ec_0 R_0}. \qquad [3]$$

The Dukhin number indicates the relative importance of ionic transport in the screening layer vs. in the bulk (1). In everything that follows, we use the nondimensionalized variables defined in Table 1.

The dimensionless and radially averaged 1D fluxes take the form

$$I = \overbrace{\pi R^2 \left(-\frac{dn_c}{dx}\right)}^{I_{\mathrm{diff}}} + \overbrace{\pi R^2 c \left(-\frac{d\phi}{dx}\right)}^{I_{\mathrm{ep}}} + Q\delta n_c + \overbrace{2\pi R k \left(-\frac{d\phi}{dx}\right)}^{I_{\mathrm{eo}}}$$

$$+ \overbrace{\frac{1}{\mathrm{Pe}_{\mathrm{osm}}}\frac{\mu_{\mathrm{EO}}}{\mu_{\mathrm{EP}}}\pi R^2 \left(-\frac{dP}{dx}\right)}^{I_{\mathrm{stm}}} + \overbrace{2\pi R k \left(\mathrm{S}\frac{d\ln c}{dx}\right)}^{I_{\mathrm{do}}} \qquad [4]$$

$$J_{\mathrm{sol}} = -\pi R^2 \left(\frac{dc}{dx} + n_c \frac{d\phi}{dx}\right) + Qc, \qquad [5]$$

$$Q = -\pi R^4 \left(\frac{dP}{dx} + \mathrm{Pe}_{\mathrm{osm}}\delta n_c \frac{d\phi}{dx}\right)$$
$$+ \pi R^2 \left[\frac{\mu_{\mathrm{EO}}}{\mu_{\mathrm{EP}}}\left(-\frac{d\phi}{dx}\right) + \frac{\mu_{\mathrm{DO}}}{D}\left(-\frac{d\ln c}{dx}\right)\right], \qquad [6]$$

which verify conservation laws

$$\frac{dI}{dx} = \frac{dJ_{\mathrm{sol}}}{dx} = \frac{dQ}{dx} = 0, \qquad [7]$$

together with the Poisson equation

$$\left(\frac{\lambda_D}{\ell}\right)^2 \frac{1}{\pi R^2}\frac{d}{dx}\left(\pi R^2 \frac{d\phi}{dx}\right) + \delta n_c = 0. \qquad [8]$$

These equations are derived in *Derivation of Eqs. 4–8: Radial Integration of PNPS Equations*; they express conservation of electric charge, solute mass, and solvent volume. In the right-hand side of Eq. **4**, the terms represent the contributions from diffusion (I_{diff}), electrophoresis (I_{ep}), bulk advective transport of the local net charge, electroosmosis (I_{eo}), streaming current (I_{stm}), and diffusioosmosis (I_{do}). Similar interpretations hold for the terms in Eq. **5**. We emphasize that we do not presuppose the overlap of Debye layers.

The mechanisms at play are described in terms of various mobilities: μ_{EP} and μ_{EO}, the electrophoretic and -osmotic mobilities; μ_{DO}, their diffusioosmotic counterpart (32); and the diffusion coefficient D, related to the electrophoretic mobility by the Einstein relation $D = \mu_{\mathrm{EP}} \times k_B T/e$. The equations also contain the Debye length $\lambda_D \equiv \sqrt{\epsilon_r \epsilon_0 k_B T/e^2 c_0}$ and ℓ, the geometric length scale characterizing the nanocapillary tip (Fig. 3). In addition to the Dukhin number (Eq. **3**), we have introduced the dimensionless parameter

$$\mathrm{Pe}_{\mathrm{osm}} \equiv \frac{R_0^2 k_B T c_0}{8\eta D}, \qquad [9]$$

which compares diffusion to a pressure-driven flow associated with the scale of an osmotic pressure $k_B T c_0$ and may accordingly be interpreted as an osmotic Péclet number. Finally, $2\pi R k$

Table 1. Model variables and their rescaled dimensionless counterparts

Variable	Notation	Rescaled
Position	x	$x \to \ell x$
Radius	R	$R \to R_0 R$
Concentration	c	$c \to c_0 c$
Charge Density	n_c	$n_c \to ec_0 n_c$
Potential	ϕ	$\phi \to (k_B T/e)\phi$
Solute flux	J_{sol}	$J_{\mathrm{sol}} \to (R_0^2 Dc_0/\ell)J_{\mathrm{sol}}$
Electric Current	I	$I \to (R_0^2 eDc_0/\ell)I$
Water flux	Q	$Q \to (R_0^2 D/\ell)Q$
Pressure	P	$P \to (8\eta D/R_0^2)P$

The length ℓ characterizes the transition between the interior of the nanopore and the reservoir (Fig. 3 and main text).
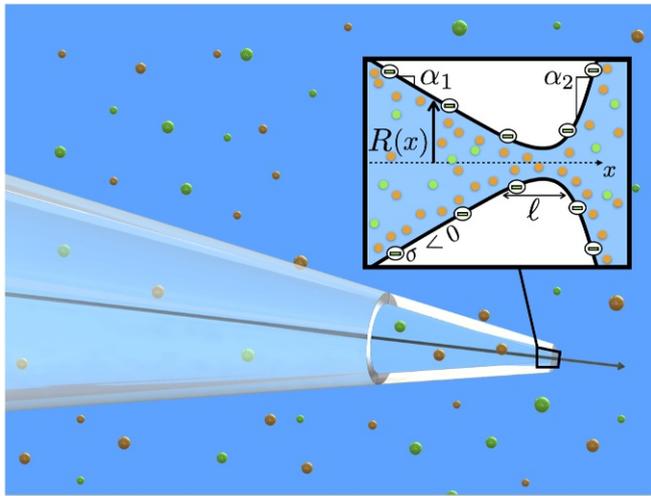
Fig. 3. A sketch of the geometry of the glass nanocapillary. *Inset* shows a zoom-in of the model geometry in the vicinity of the tip. The radius is taken to vary between two regions of linear variation over a length-scale ℓ as indicated, and these regions are characterized by radial slopes $\alpha_1 = 0.1$ in the interior and $\alpha_2 = 200$ in the exterior.

is the local cross-sectionally integrated electroosmotic conductivity, with $k \equiv 16\mathrm{Du}_0\mathrm{Pe}_{\mathrm{osm}}(\lambda_D/R_0)^2$. The values of all of the dimensionless parameters governing the solution were estimated for the experiments presented above: $\mathrm{Du}_0 \simeq 0.5$, $\lambda_D/R_0 \simeq 0.05$, $\lambda_D/\ell \simeq 0.1$, $\mu_{\mathrm{EO}}/\mu_{\mathrm{EP}} \simeq 0.2$, $\mu_{\mathrm{DO}}/D \simeq 1$, $\mathrm{Pe}_{\mathrm{osm}} \simeq 10$, and $\ell/R_0 \approx 0.5$. Additionally, the interior radial slope is $\alpha_1 \approx \tan(5°) \approx 0.1$. These parameters are used in all of the numerical calculations presented below.

The model geometry is shown in Fig. 3. The radius is taken to vary continuously between two linear regions: The upstream region of slope $dR/dx = -\alpha_1$, representing the nanopore interior, and the downstream region of slope $dR/dx = +\alpha_2 = 200$, representing the rapid divergence of the radius as the downstream reservoir is approached. The transition between radial slopes occurs continuously over a length ℓ (Fig. 3 and *Model Geometry*). The boundary conditions are imposed in the reservoirs at $x = \pm\infty$: $\phi(x \to +\infty) = P(x \to +\infty) = 0$, $\phi(x \to -\infty) = \Phi$, $P(x \to -\infty) = \mathrm{Pe}_P$, together with conditions on the charge and salt concentration $c(x \to \pm\infty) = 1$ and $n_c(x \to \pm\infty) = 0$. In the preceding, we have introduced the dimensionless driving forces

$$\Phi \equiv e\Delta V/k_B T \approx \Delta V/25\,\mathrm{mV}$$
$$\mathrm{Pe}_P \equiv R_0^2 \Delta P/8\eta D \approx \Delta P/6\,\mathrm{mbar}. \qquad [10]$$

Results

The coupled transport equations given above, Eqs. **4**–**7**, were solved numerically, and the results for the response of the current to applied voltage and pressure are reported in Fig. 4. The results for the conductance are reported in Fig. 2 C and D.

Crucially, this theoretical framework reproduces all of the essential qualitative features of the experiments. Comparing the experimental results—Figs. 1 C and D and 2 A and B—to the theoretical predictions—Figs. 2 C and D and 4—, we see that we successfully recover a strong, nonlinear dependence of the ionic conduction on pressure (Fig. 2 C and D), resulting in a highly sensitive response of the pressure-induced current I_P to pressure (Fig. 4B). We note that, in the model, the applied forcings are larger than those in the experiments. This was necessary to recover the correct degree of rectification in the IV curves

and is presumably due to the simplifying one-dimensionality of our model.

Furthermore, the prediction for the Péclet dependence of the current I_P shown in Fig. 4B is successfully described by Eq. **1**, in full agreement with the experimental results shown in Fig. 1D. This demonstrates that the experimental behavior $I_P \sim \Delta P^{1/2}$ measured for low pressure drop is fully recovered by the model, indicating a strong sensitivity to applied pressure for small pressures. Finally, the theoretical IV curves are observed to linearize as pressure is increased, in accordance with the experimental observations shown in Fig. 1C, with the conductance for all voltages approaching the conductance at zero voltage drop, $\Phi = 0$ (Fig. 4A). The apparent offset in the linear streaming current for large applied pressures is asymmetric in applied voltage, growing much more quickly for negative than for positive values of Φ, in full agreement with its experimental counterpart.

Discussion: The Deformation of the SCZ

We now show that this nontrivial behavior originates in the sensitivity of the SCZ to the balance between electrical and mechanical forcing. We first note that at equilibrium the present system exhibits a nonvanishing net charge density (δn_c, Eq. **2**) profile. Solving the above transport equations for $I = J_{\mathrm{sol}} = Q = 0$, we find that the net charge density at equilibrium, $\delta n_c^{\mathrm{equ}}$, is nonzero in the conical system and obeys an implicit linear relationship with the Dukhin number,

$$G_b\left(\frac{\ell}{\lambda_D}\right)^2 \int_{-\infty}^{+\infty} \frac{\mathrm{d}x}{\pi R^2} \int_{-\infty}^{x} \mathrm{d}x'\, \pi R^2 \delta n_c^{\mathrm{equ}} = 2\pi \frac{\ell}{R_0}\alpha_1 \mathrm{S}\,\mathrm{Du}_0,$$

$$[11]$$

where $G_b = \left[\int_{-\infty}^{+\infty} \mathrm{d}x/\pi R^2\right]^{-1}$ is the (dimensionless) bulk electrophoretic conductance. (Note that a more detailed derivation of this equation and those following is given in *Derivation of Eqs. 11 and 12*, *Derivation of Eq. 13*, and *Derivation of Eq. 14*.) This result may be interpreted in terms of the buildup of a Donnan potential inside the conical nanocapillary, which in the present conditions (a nonoverlapping Debye layer) disappears as the capillary angle α_1 vanishes and a simple cylindrical geometry is obtained.
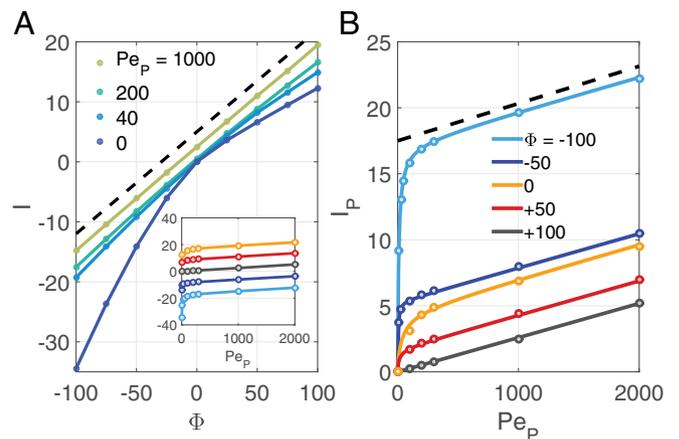
Fig. 4. Model-derived response of the ionic current I to applied voltage Φ and pressure Pe_P in a conical quasi–one-dimensional geometry (Fig. 3). (*A*) IV curves for increasing values of Pe_P, as indicated in the key. *Inset* shows the current as a function of Pe_P for several different values of Φ, colored according to the key in *B*. (*B*) Additional current induced by applied pressure, I_P, as a function of Pe_P for several different values of Φ, as indicated in the key. In *B*, the model predictions are fitted according to Eq. **1**, similar to Fig. 1 for the experimental data (with ΔP replaced by the Péclet number Pe_P). The slope of the dashed black line in *A* indicates the value of G_0, and that in *B* indicates the value of $\mathrm{S}_{\mathrm{stm}}$ (Eq. **14**).

Under applied voltage and pressure drops, this equilibrium SCZ is modified. Interestingly, one may still obtain an explicit integral relationship between the current and the charge imbalance:

$$I = G_b \left[\Phi - \left(\frac{\ell}{\lambda_D} \right)^2 \int_{-\infty}^{+\infty} \frac{dx}{\pi R^2} \int_{-\infty}^{x} dx' \pi R^2 \left[\delta n_c - \delta n_c^{equ} \right] \right]. \tag{12}$$

In practice, this equation is obtained by first solving the Poisson equation (Eq. **8**) for the electric flux at $x = -\infty$ and then relating this to the ionic current by examining the limiting behaviors of the flux equations (Eqs. **4–6**).

This result explicitly confirms that the nonlinear response results from the deformation of the SCZ under these driving forces. From the model results, we learn that for small Péclet number $\mathrm{Pe}_P \to 0$, the current is dominated locally by the electrophoretic and electroosmotic responses. On the other hand, at large Péclet number, the linearization of the IP response is found to correspond to an increase in importance of the local streaming current, such that the current is dominated by the local electrophoretic, electroosmotic, and streaming current responses. We discuss each of these two regimes in turn.

Small Péclet Regime. In this regime, the striking result is the dramatic sensitivity of the conductance to applied pressure. As suggested by Eq. **1**, the current I_P exhibits a nonanalytic square-root dependence on pressure drop (or Péclet number) in this regime, so that the model predicts $G \sim \Delta P^{1/2}$. The conductance in this small Péclet regime may be estimated by retaining only the electrophoretic and electroosmotic terms in the expression for the ionic current (Eq. **4**). Integrating in x, one finds for the apparent conductance $G = I/\Delta V$,

$$G = \left[\int_{-\infty}^{+\infty} \frac{dx}{\pi R^2 \left(c + \frac{2k}{R} \right)} \right]^{-1}, \tag{13}$$

where the (nonlinear) pressure dependence is hidden in the concentration profile $c(x; \mathrm{Pe}_P, \Phi)$. The above result for the apparent conductance (Eq. **13**) shows that for small Péclet number, the variation in the apparent conductance with pressure drop, $G(\mathrm{Pe}_P)$, may be understood in terms of the pressure-induced variations in the concentration profile $c(\mathrm{Pe}_P)$ relative to equilibrium. Concentration profiles are plotted in *Concentration and Cumulative Charge Profiles* and Fig. S3. These profiles exhibit a strong sensitivity to applied pressure when $\mathrm{Pe}_P < 50$, with the concentration everywhere relaxing to the reservoir value as the linearizing Péclet number $\mathrm{Pe}_P^{\mathrm{lin}} \approx 300$ is approached.

The equivalence of Eq. **13** and the more general Eq. **12** in describing the current response at low Pe_P implies a direct relationship between the net spatial charge δn_c and the concentration field. This is illustrated in Fig. S3, where we have also plotted profiles of the cumulative charge in the nanopore, $\delta q \equiv \int_{-\infty}^{x} dx \pi R^2 \delta n_c$. The structural similarity between the cumulative charge and the excess concentration relative to the reservoir value $\delta c \equiv c - 1$ is immediately apparent.

This suggests a back-of-the-envelope argument to account for the square-root variation of the conductance with Péclet number, $G \sim \mathrm{Pe}_P^{1/2}$, highlighted in Eq. **1**. Under a pressure drop, one may anticipate a simple mechanical balance for the SCZ between the electrostatic and pressure forces. This typically takes the form $\delta q \times E_{\mathrm{app}} \sim R_0^2 \Delta P$, where δq is the variation of the cumulative charge in the SCZ and E_{app} is the variation in the induced electric field, under the applied pressure. Equivalently, one may interpret the force balance in terms of a balance between the Maxwell stress and the applied pressure:

$\frac{1}{2} \epsilon E_{\mathrm{app}}^2 \sim \Delta P$. The equivalence of these perspectives requires that the cumulative charge in the SCZ be proportional to the induced electric field, $\delta q \sim E_{\mathrm{app}}$, in agreement with the Poisson equation, Eq. **8**. Solving for δq yields $\delta q \sim \pm \sqrt{\Delta P}$ (depending on the sign of the applied voltage drop) or, in dimensionless variables, $\delta q \sim \pm \sqrt{\mathrm{Pe}_P}$. Furthermore, as noted above, the variation in the concentration field is found to scale with the cumulative charge. We thus have $\delta c \sim \delta q \sim \pm \sqrt{\mathrm{Pe}_P}$. From Eq. **13**, this variation in the concentration leads to a modification of the conductance scaling as $\delta G(\mathrm{Pe}_P) \sim \pm \sqrt{\mathrm{Pe}_P}$ for small Péclet number.

While this scaling is established a posteriori, it recovers the nonanalytic square-root correction to the conductance in the Péclet number, in full agreement with the corresponding variation observed in the experiments and theory, as shown in Fig. 2. It also suggests that the origin of the nonanalyticity is in the contribution to the mechanical balance on the SCZ of the Maxwell stress tensor and its quadratic dependence on the electric field. Interestingly, this dependence is expressed for the present conical geometry, but disappears for cylindrical geometries with constant radius.

Large Péclet Regime. In this regime, the current response is linear in applied voltage and pressure (Figs. 1 and 4). This puzzling behavior can be rationalized analytically by noting that the current is dominated by the electrophoretic, electroosmotic, and streaming contributions. Under these conditions, one can deduce the analytical expression for the current as

$$I = G_0 \left(\Phi + \gamma \frac{\mu_{\mathrm{EO}}}{\mu_{\mathrm{EP}}} \frac{\mathrm{Pe}_P}{\mathrm{Pe}_{\mathrm{osm}}} \right) \equiv G_0 \Phi + \mathrm{S}_{\mathrm{stm}} \mathrm{Pe}_P, \tag{14}$$

where $\gamma \equiv \left[\int_{-\infty}^{+\infty} dx/\pi R^4 \left(1 + \frac{2k}{R} \right) \right] \Big/ \left(\int_{-\infty}^{+\infty} dx/\pi R^4 \right)$ is an order-one constant. We have also introduced $G_0 = \left[\int_{-\infty}^{+\infty} dx/\pi R^2 \left(1 + \frac{2k}{R} \right) \right]^{-1}$, the bulk electrophoretic conductance G_b enhanced by the electroosmotic contribution (1).

This result, although formally clear, is striking in several aspects. First, in this regime, the current is shown to be linear in both voltage drop (Φ) and pressure drop (Pe_P), in full agreement with the experimental results. Furthermore, the conductance and streaming current take their linear response values, i.e., those calculated at vanishing voltage and pressure drop. Indeed, with the exception of small corrections induced by the inclusion of the electroosmotic contribution, the streaming conductance $\mathrm{S}_{\mathrm{stm}} \equiv \partial I/\partial \mathrm{Pe}_P = G_0 \gamma (\mu_{\mathrm{EO}}/\mu_{\mathrm{EP}})(1/\mathrm{Pe}_{\mathrm{osm}}) \approx G_b (\mu_{\mathrm{EO}}/\mu_{\mathrm{EP}})(1/\mathrm{Pe}_{\mathrm{osm}})$ takes the value obtained by assuming that the streaming current alone drives the local current response at high pressure everywhere in the nanopore.

Conclusions and Perspectives

Our results demonstrate that the ionic conductance of a conical nanopore can be tuned very sensitively by the applied pressure. An increase or decrease of the conductance by up to 100% can be achieved under slight variations in the pressure, stimulating a transition from a high to a low conductance state (or vice versa). Furthermore, the pressure dependence of the conductance is found to be nonanalytical in the applied pressure drop, while a linear behavior is counterintuitively recovered only at high pressure. This strongly nonlinear transport behavior is fully captured by a theoretical framework accounting for the deformation of the SCZs under the coupled mechanical and electrical drivings.

The possibility to mechanically tune conduction mimics a mechanical transistor functionality, with the pressure opening or closing conductance channels. In organisms, the

APPLIED PHYSICAL SCIENCES

mechanosensitive response of dedicated pores is of crucial importance in preventing fatal osmotic shocks by activating channels under hydrostatic or diffusioosmotic forces (21–23). Here the response to pressure is of a different type, as the pressure is found to tune rather than open or close the electric conduction channels. However, it would be interesting to extend the present study to the osmotic response induced by a difference in salinity across the nanopore. Such a salt concentration difference results in a Nernst potential difference which, according to our present analysis, will couple to the pressure response. Furthermore, salinity differences lead to diffusioosmotic forces which will enter the mechanical balance on top of electrical and mechanical forces studied here (23). This suggests that more complex nonlinear responses are expected in such situations, opening the possibility to tune both ionic and solute flux responses under a variety of stimuli.

We conclude by noting that such a mechanosensitive behavior may also find applications in the context of membrane science, where the possibility to activate or inhibit the electric conduction by small pressure stimuli could be of interest for various applications. For example, in the context of osmotic (blue) energy, the maximum achievable power is proportional to the electric resistance of the membrane (20), and the present nonlinear couplings may allow for mechanical tunability of the extracted power.

Altogether the pressure-sensitive conduction constitutes an elementary building block which we hope will allow for development of new active functionalities mimicking the advanced machines (33) existing in Nature.

Materials and Methods

Nanocapillary profiles and tip diameters were determined using scanning electron microscopy (SEM). (Fig. 1B and Fig. S1). During the experiments, both ends of the nanocapillary were submerged in reservoirs containing Ag/AgCl electrodes and the same aqueous solution of KCl. Ionic currents were then measured between the electrodes for fixed applied voltages (applied via the upstream electrode; Fig. 1A and Fig. S2) and pressures (applied in the upstream reservoir). The current response was recorded in the range $-400 < \Delta V < +400$ mV and $0 < \Delta P < 1,500$ mbar. Further details of the experimental procedure and setup are given in SI Materials and Methods.

1. Bocquet L, Charlaix E (2010) Nanofluidics, from bulk to interfaces. *Chem Soc Rev* 39:1073–1095.
2. Schoch RB, Han J, Renaud P (2008) Transport phenomena in nanofluidics. *Rev Mod Phys* 80:839–883.
3. Misakian M, Kasianowicz JJ (2003) Electrostatic influence on ion transport through the αHL channel. *J Membr Biol* 195:137–146.
4. Schiedt B, Healy K, Morrison AP, Neumann R, Siwy Z (2005) Transport of ions and biomolecules through single asymmetric nanopores in polymer films. *Nucl Instrum Methods Phys Res Sect B* 236:109–116.
5. Rankin DJ, Huang DM (2016) The effect of hydrodynamic slip on membrane-based salinity-gradient-driven energy harvesting. *Langmuir* 32:3420–3432.
6. Ren Y, Stein D (2008) Slip-enhanced electrokinetic energy conversion in nanofluidic channels. *Nanotechnology* 19:195707.
7. Siria A, et al. (2013) Giant osmotic energy conversion measured in a single transmembrane boron nitride nanotube. *Nature* 494:455–458.
8. van der Heyden FHJ, Bonthuis DJ, Stein D, Meyer C, Dekker C (2006) Electrokinetic energy conversion efficiency in nanofluidic channels. *Nano Lett* 6:2232–2237.
9. Picallo CB, Gravelle S, Joly L, Charlaix E, Bocquet L (2013) Nanofluidic osmotic diodes: Theory and molecular dynamics simulations. *Phys Rev Lett* 111:244501.
10. Shockley W (1949) The theory of p-n junctions in semiconductors and p-n junction transistors. *Bell Labs Tech J* 28:435–489.
11. Cheng LJ, Guo LJ (2010) Nanofluidic diodes. *Chem Soc Rev* 39:923–938.
12. Chun H, Chung TD (2015) Iontronics. *Annu Rev Anal Chem* 8:441–462.
13. Boon N, de la Cruz M (2015) 'Soft' amplifier circuits based on field-effect ionic transistors. *Soft Matter* 11:4793–4798.
14. Sun G, Senapati S, Chang HC (2016) High-flux ionic diodes, ionic transistors and ionic amplifiers based on external ion concentration polarization by an ion exchange membrane: A new scalable ionic circuit platform. *Lab Chip* 16:1171–1177.
15. Lan WJ, et al. (2016) Voltage-rectified current and fluid flow in conical nanopores. *Acc Chem Res* 49:2605–2613.
16. Laohakunakorn N, et al. (2013) A Landau-Squire nanojet. *Nano Lett* 13:5141–5146.
17. Laohakunakorn N, Keyser UF (2015) Electroosmotic flow rectification in conical nanopores. *Nanotechnology* 26:275202.
18. Wu X, Rajasekaran PR, Martin CR (2016) An alternating current electroosmotic pump based on conical nanopore membranes. *ACS Nano* 10:4637–4643.
19. Siwy Z, Fuliński A (2002) Fabrication of a synthetic nanopore ion pump. *Phys Rev Lett* 89:198103.
20. Siria A, Bocquet M-L, Bocquet L (2017) New avenues for the large-scale harvesting of blue energy. *Nat Rev Chem* 1:0091.
21. Perozo E, Cortes DM, Sompornpisut P, Kloda A, Martinac B (2002) Open channel structure of MscL and the gating mechanism of mechanosensitive channels. *Nature* 418:942–948.
22. Vásquez V, Sotomayor M, Cordero-Morales J, Schulten K, Perozo E (2008) A structural mechanism for MscS gating in lipid bilayers. *Science* 321:1210–1214.
23. Bonthuis DJ, Golestanian R (2014) Mechanosensitive channel activation by diffusio-osmotic force. *Phys Rev Lett* 113:148101.
24. Tybrandt K (2017) Exploring the potential of ionic bipolar diodes for chemical neural interfaces. *Soft Matter* 13:8171–8177.
25. Karnik R, Castelino K, Majumdar A (2006) Field-effect control of protein transport in a nanofluidic transistor circuit. *Appl Phys Lett* 88:123114.
26. Schasfoort RB, Schlautmann S, Hendrikse J, van den Berg A (1999) Field-effect flow control for microfabricated fluidic networks. *Science* 286:942–945.
27. Chua L (2013) Memristor, Hodgkin–Huxley, and edge of chaos. *Nanotechnology* 24:383001.
28. Lan WJ, Holden DA, White HS (2011) Pressure-dependent ion current rectification in conical-shaped glass nanopores. *J Am Chem Soc* 133:13300–13303.
29. White HS, Bund A (2008) Ion current rectification at nanopores in glass membranes. *Langmuir* 24:2212–2218.
30. Zembala M (2004) Electrokinetics of heterogeneous interfaces. *Adv Colloid Interface Sci* 112:59–92.
31. Iler RK (1979) *The Chemistry of Silica: Solubility, Polymerization, Colloid and Surface Properties, and Biochemistry* (Wiley, Hoboken, NJ).
32. Ajdari A, Bocquet L (2006) Giant amplification of interfacially driven transport by hydrodynamic slip: Diffusio-osmosis and beyond. *Phys Rev Lett* 96:186102.
33. Fu YM, et al. (2017) Hodgkin–Huxley artificial synaptic membrane based on protonic/electronic hybrid neuromorphic transistors. *Adv Biosyst* 2:1700198.